Novel Clustering Schemes for Full and Compact Polarimetric SAR Data: A Case Study for Rice Phenology Characterization

Subhadip Dey[a,*], Avik Bhattacharya[a], Debanshu Ratha[a], Dipankar Mandal[a], Heather McNairn[b], J. M. Lopez-Sanchez[c], Y. S. Rao[a]

[a]*Microwave Remote Sensing Lab, CSRE, Indian Institute of Technology Bombay, Mumbai, India*
[b]*Ottawa Research and Development Centre, Agriculture and Agri-Food Canada, Canada*
[c]*University of Alicante, Alicante, Spain*

Abstract

Information on rice phenological stages from Synthetic Aperture Radar (SAR) images is of prime interest for in-season monitoring. Often, prior in-situ measurements of phenology are not available. In such situations, unsupervised clustering of SAR images might help in discriminating phenological stages of a crop throughout its growing period. Among the existing unsupervised clustering techniques using full-polarimetric (FP) SAR images, the eigenvalue-eigenvector based roll-invariant scattering-type parameter, and the scattering entropy parameter are widely used in the literature. In this study, we utilize a unique target scattering-type parameter, which jointly uses the Barakat degree of polarization and the elements of the polarimetric coherency matrix. In particular, the degree of polarization attributes to scattering randomness from a target. The scattering randomness in crops increases with advancements in its growth stages due to the development of branches and

*Corresponding author: Subhadip Dey (sdey2307@gmail.com)

foliage. Hence, the degree of polarization varies with changes in the crop growth stages. Besides, the elements of the coherency matrices are directly related to the crop geometry as well as soil and crop water content. Therefore, this complementarity information captures the scattering randomness at each crop growth stage while taking into account diverse crop morphological characteristics. Likewise, we also utilize an equivalent parameter proposed for compact-polarimetric (CP) SAR data. These scattering-type parameters are analogous to the Cloude-Pottier's parameter for FP SAR data and the ellipticity parameter for CP SAR data. Besides this, we also introduce new clustering schemes for both FP and CP SAR data for segmenting diverse scattering mechanisms across the phenological stages of rice. In this study, we use the RADARSAT-2 FP and simulated CP SAR data acquired over the Indian test site of Vijayawada under the Joint Experiment for Crop Assessment and Monitoring (JECAM) initiative. The temporal analysis of the scattering-type parameters and the new clustering schemes help us to investigate detailed scattering characteristics from rice across its phenological stages.

Keywords: Unsupervised clustering, Entropy, RADARSAT-2, Crop monitoring, PolSAR, Roll-invariant parameter

---

1. Introduction

Variations in crop phenological stages can be characterized by Synthetic Aperture Radar (SAR) data due to its high sensitivity to the dielectric and geometrical structure of the canopy. However, depending on the frequency of the transmitted electromagnetic (EM) wave, the interaction with crop

canopy layers and the underlying soil varies significantly (Davidson et al., 2000). Previous studies reported that phenological changes could be adequately captured with high-frequency SAR sensors utilizing backscattered information from vegetation canopy (Wiseman et al., 2014; De Bernardis et al., 2015; McNairn and Shang, 2016; McNairn et al., 2018). In general, the SAR backscatter signal might be affected by the underlying surface during early vegetative growth stages when the canopy was sparse and open (Paloscia, 2002).

In particular, for rice monitoring, Le Toan et al. (1989) investigated the temporal backscatter response of σ^0_{HH} and σ^0_{VV} from dual-polarized airborne SAR data. It was noticed that the dynamic ranges of σ^0_{HH} and σ^0_{VV} for rice fields were higher (up to $\approx$10 dB) than any other crop fields, possibly due to the flooding condition in those fields. In another study, Kurosu et al. (1995) reported that ERS-1 C-band SAR data had a second-order polynomial relationship of the backscatter values with the number of days after transplanting. Besides, a high correlation of rice biomass with radar backscatter values was also apparent. Although these satellites have low revisit time and coarse resolution, the temporal pattern of HH and VV backscatter has been shown to adequately capture the phenological growth of rice (Le Toan et al., 1997; Koay et al., 2007; Bouvet et al., 2009). The discrimination of rice fields from non-rice fields was conducted using the C-band HH/VV ratio, which shows a distinct variation from the beginning of the season until the crop maturity stage. Besides, several other SAR systems (e.g., RADARSAT-2, ALOS-2, TerraSAR-X) have been exploited for crop growth monitoring by correlating the backscatter changes to the crop morphological characteristics (Canisius

et al., 2018; Torbick et al., 2017).

One of the primary parameters associated with the changes in the SAR backscatter coefficient is the crop canopy distribution (e.g., tillers, leaves, and panicles) at each phenological stage. Moreover, this distribution in the crop fields also leads to randomness in scattering (Yuzugullu et al., 2015). In such situations, polarimetric entropy (H) is an important parameter to quantify this randomness. In Cloude and Pottier (1997), an unsupervised classification scheme ($H/\overline{\alpha}$) was proposed using H and the average scattering-type parameter ($\overline{\alpha}$).

Lopez-Sanchez et al. (2011) reported the importance of the $H/\overline{\alpha}$ plane to discriminate phenological stages of rice along with the temporal correlation of HH and VV and their ratio. The clustering results show that at the beginning of the cultivation period of rice, the data cluster was denser in the region with medium entropy and low alpha, which was primarily due to the presence of sparse vegetation in the fields. However, at the advanced phenological stages, the cluster density shifted towards the region of high entropy and high alpha in the $H/\overline{\alpha}$ plane.

In another study, Lopez-Sanchez et al. (2012) utilized the dominant scattering-type information (α_1) instead of $\overline{\alpha}$. In this study, the temporal behaviour of α_1 and the scattering entropy was shown with the phenological stages of rice. At the initial stage, α_1 and entropy were both within low to medium values, and they jointly increased during the plant emergence stage. During the advanced vegetative stage, both parameters show the dominance of multiple scattering from the fields. In contrast, at the harvest stage, $\alpha_1 < 30^\circ$ and the scattering entropy remained high due to the field roughness condition.

Praks et al. (2009) proposed alternative scattering-type and randomness parameters equivalent to $\overline{\alpha}$ and H for clustering PolSAR data. These parameters can be directly obtained from the elements of the coherency matrix without utilizing the eigenvalues and the eigenvectors. It was shown that instead of $\overline{\alpha}$ and H, the surface scattering fraction and the scattering diversity that are equivalent polarimetric descriptors can be utilized for classification, visualization, or interpretation. Later, Yin et al. (2015) proposed a new parameter, α_B, defined by the co-polarization ratio and their coherence to capture various scattering mechanisms. This new parameter was able to distinguish scattering from oriented and randomly distributed targets. In their study a new $\Delta\alpha_{\mathrm{B}}/\alpha_{\mathrm{B}}$ plane was proposed which showed better separation capability than the $H/\overline{\alpha}$ clustering plane. It was also stated that the stability of the proposed method was better with multi-temporal SAR data.

In another work, Ratha et al. (2019) proposed a roll-invariant scattering-type parameter (α_{GD}), the helicity parameter (τ_{GD}), and the purity parameter (P_{GD}) using a geodesic distance between two Kennaugh matrices. A new P_{GD}/α_{GD} unsupervised classification scheme is proposed whic is analogous to $H/\overline{\alpha}$. However, the P_{GD}/α_{GD} clustering plane showed better performance than earlier proposed schemes.

The study using compact-polarimetric (CP) SAR data holds promise due to the upcoming constellation of satellites such as the Canadian RADARSAT Constellation Mission (RCM), SAOCOM (TOPSAR with experimental CP-mode), and the NISAR (the NASA-ISRO SAR) L- and S-band mission. Similar to the full-polarimetric (FP) case, scattering-type clustering assessment using compact polarimetric (CP) SAR data and its decomposition

parameters (Raney, 2007; Cloude et al., 2011; Raney et al., 2012) are lately gaining interest (Ainsworth et al., 2009; Charbonneau et al., 2010; Ballester-Berman and Lopez-Sanchez, 2011; Sabry and Vachon, 2013). Brisco et al. (2013) assessed hybrid-compact, circular, and linear polarimetric SAR data for rice and wetlands mapping. Also, different dual-channel combinations and $m - \delta$ decomposition parameters for CP data were assessed in their study, where the classification accuracy for CP data was comparatively better than linear dual-polarimetric SAR data.

Lopez-Sanchez et al. (2014) used the radar backscatter coefficients and the $H/\overline{\alpha}$ plane to investigate the dynamics of rice phenological changes for full, dual, and compact polarimetric SAR data. In this study, the dominant scattering-type parameter (α_s) for CP data is used instead of $\overline{\alpha}$. For CP data, the entropy, in particular, is equivalent to the Barakat degree of polarization. It was noticed that the pattern of α_s was similar for full, dual, and compact polarimetric SAR data for rice crops. Alongside this, it was also observed that α_s precisely provides similar information like the FP mode, throughout the phenological cycle of rice. On the contrary, among other decomposition parameters, δ provides quite noisy information.

Subsequently, Yang et al. (2014) showed improved classification accuracy in discriminating transplanted and direct-sown rice fields. In this study, the use of the $m - \chi$ decomposition parameters along with α_s, the degree of polarization (m), relative phase (δ) and conformity coefficient (μ) improved the classification accuracy from 88 % to 95 %. Besides, the classification accuracy confirmed the advantage of CP data over other dual-polarized SAR data. Several other studies (Xie et al., 2015; Uppala et al., 2015; Guo et al.,

2018; Kumar et al., 2020) also indicated the potential of CP SAR data for rice mapping and monitoring.

Recently, Yin et al. (2019) proposed a new parameter, α_{BCP}, for improvement in the clustering results for land-cover features. In particular, α_{BCP} is rotation-invariant and $\Delta\alpha_{BCP}/\alpha_{BCP}$ resembles the existing $\Delta\alpha_B/\alpha_B$ clustering for FP SAR data. However, the differences between α_{BCP} and α_B depend on the polarization of the received wave. Moreover, the derivation of specific scattering models is needless for separate CP modes. It was also observed that circular CP data provides almost similar results as FP data for various scattering targets.

The literature, as mentioned above, provides a vital foundation for the utilization of H and the scattering-type parameters (i.e., $\overline{\alpha}$ and α_s) for rice crop monitoring and mapping using FP and CP SAR data. Nevertheless, these techniques are formulated either by fitting scattering models or by diagonalizing the coherency (or covariance) matrix of the received wave. Hence, these techniques might miss the received antenna basis invariant information while characterizing various targets. The importance of the received antenna basis invariant information in terms of the degree of polarization helps to effectively exploit complete information from SAR data (Touzi et al., 2015, 2018). In this regard, a new scattering-type parameter is derived by jointly using the received antenna basis invariant information and elements of coherency (or, covariance) matrix for both FP and CP SAR data.

In this study, our main objective is to characterize changes in scattering mechanisms utilizing the temporal series of full- and compact polarimetric SAR data across the growth stages of rice. In this regard, we propose

roll-invariant scattering-type parameters using the received antenna basis invariant information along with the elements of the coherency (or, covariance) matrices. The received antenna basis invariant information, i.e., in particular, the Barakat degree of polarization (Barakat, 1977, 1983) is useful to capture changes in scattering randomness due to crop foliage development. At the same time, the elements of the coherency (or, covariance) matrices provide information about crop canopy geometry as well as the soil and vegetation water content. Hence, jointly utilizing these information might be helpful in better monitoring the crop growth stages. Alongside this, we present a comparative study of the performance of novel clustering schemes for FP and CP data for rice phenology mapping.. It is noteworthy that the formulation of this new scattering-type parameter is equivalent for both FP and CP SAR data. This parameter is comparable to the Cloude and Pottier $\overline{\alpha}$ (Cloude and Pottier, 1997) for FP. It may be noted that θ_{FP} consider the Barakat degree of polarization in its formulation unlike $\overline{\alpha}$, and hence, it additionally utilizes the received antenna basis invariant information. We have proposed new clustering schemes using θ_{FP} and θ_{CP} along with H for both FP and CP SAR data, respectively. Unlike the H/α plane, the proposed segmentation scheme utilizes a polar representation, which offers a natural choice. Suitable entropy apportionment (radially) together with angular extent of $\theta_X \in [-90^\circ, 90^\circ]$ (where X is either FP or CP) provides a reliable target discrimination strategy. The segmentation scheme produces 12 feasible clustering zones that better characterize natural and human-made targets. The usefulness and performance of the scattering-type parameters θ_{FP} and θ_{CP}, along with the new clustering schemes, are assessed by utilizing them with

the time-series C-band RADARSAT-2 data for monitoring rice.

2. Study area and dataset

The study area is located near Vijayawada in the state of Andhra Pradesh, India ($16°24'6.2''N, 8°41'2.4''E$) as shown in Figure 1 (Mandal et al., 2019). The climatic zone of this area varies from sub-humid to humid, with mostly clayey soil texture. Areal coverage of this test site is $\approx 25 \times 25\,\mathrm{km}^2$. Rice is one of the primary and major crops cultivated in this area. The sowing period of rice varies from mid of June to mid of July depending on the variety and cultivation practices. Majorly, the cultivation starts after the pre-monsoon rain and is harvested during mid-December. The average size of each field was $\approx 60 \times 60\,\mathrm{m}^2$, and in each field, two sampling locations were chosen for in-situ measurements. Information about the crop growth stages, management practices, and biophysical parameters was noted during the field campaign from June to December 2018.

A total number of 14 in-situ field measurements were considered in this study. We measured soil moisture at each field in two sampling locations, arranged in two parallel transects along the row direction. The separation between each transect was $\approx 80\,\mathrm{m}$. We measured the pointwise soil moisture using theta-probe. Nevertheless, the soil underlying the rice crops was saturated during the majority of the growth stages due to irrigation and rainfall events. We measured vegetation samples at two points of each field due to the spatial heterogeneity within the field, which is due to the irregular growth pattern of rice. Vegetation sampling included the measurement of PAI, plant height, and phenology through non-destructive methods. The PAI is mea-

sured using the notion of hemispherical digital photography. During each measurement day, we took ten photos along two transects which are separated by 2m in each sampling point, using a wide-angle lens mounted on a digital camera. All images were post-processed using the CanEYE software to provide an estimate of PAI. The overall phenology of rice is usually expressed with three major stages: vegetative, reproductive, and mature (or ripening). The statistics of bio-physical and soil parameters are given in Table 1.

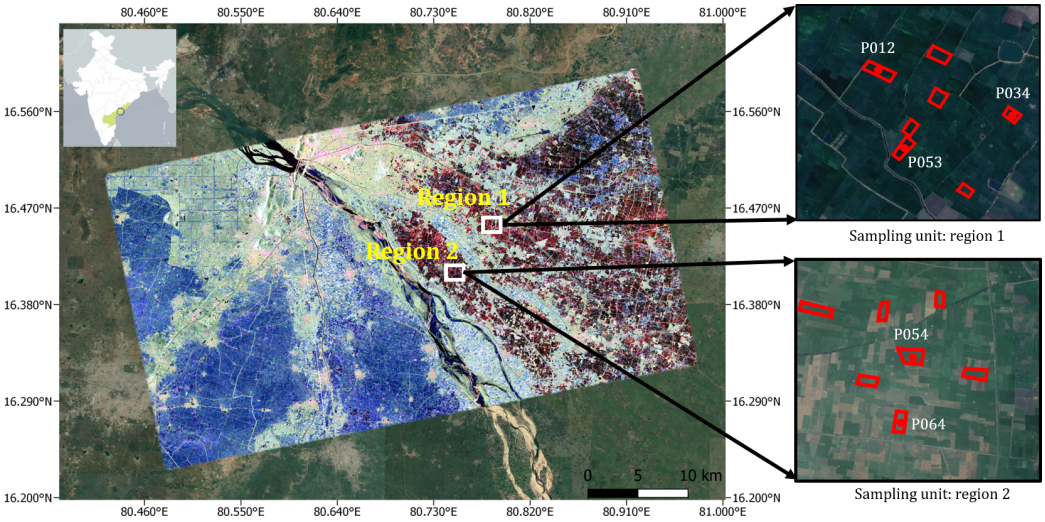

Figure 1: The Google Earth image of the JECAM test site over Vijayawada, India is overlaid with a Pauli RGB image obtained from SAR data acquired on 29 Jul 2018. The samples from region 1 and 2 are used for temporal analysis and clustering. The distribution of five in-situ data points is shown in the sampling unit of region 1 and region 2.

3. Satellite data pre-processing

We acquired RADARSAT-2 images in Fine Quad (FQ) wide mode from July to November 2018 over the test site as shown in Table 2. We then apply a multi-look factor of 2×3 pixels in the range and azimuth directions,

Table 1: Statistics (mean ± standard deviation) of bio-physical and soil parameters at different phenology stages of rice. Here, PH: plant height, PAI: plant area index, SM: soil moisture and Nan: Not a number

Date	**PH** (cm)	**PAI** ($m^2\,m^{-2}$)	**SM(%)**	**Growth stage**
05/07/2018	Nan	Nan	35.92 ± 6.6	Bare field
29/07/2018	26.30 ± 5.21	0.40 ± 0.20	Saturated	Early tillering
22/08/2018	46.26 ± 9.12	1.76 ± 0.26	Saturated	Advanced tillering
09/10/2018	92.16 ± 5.76	4.03 ± 0.20	Saturated	Flowering
02/11/2018	95.93 ± 7.76	4.06 ± 0.16	47.60 ± 0.42	Early dough
26/11/2018	98.32 ± 6.82	3.86 ± 0.22	45.16 ± 6.04	Maturity

respectively, to generate ≈ 15m square pixel images. In general, the parcel sizes in this test area are small. However, during rice cultivation, many fields are cultivated alongside the field boundaries. Therefore, the fields seem to be quasi-homogeneous, depending on cultivation practices. Since the area is quasi-homogeneous, we apply a 3×3 boxcar filter (Lee and Pottier, 2009) to each coherency matrix ($\mathbf{T}$) in the images for speckle reduction. Furthermore, we generate simulated compact polarimetric (CP) SAR data from the FP data with 0° orientation angle and −45° ellipticity angle. We co-register all FP and CP images with the RMSE $\leq 0.25\,\mathrm{m}$.

4. Methodology

In this section, we present the newly proposed scattering-type parameters for both full- and compact-pol SAR data (Dey et al., 2020) for monitoring rice crop. Alongside this, we propose an unsupervised clustering scheme utilizing these new parameters along with the scattering entropy parameter (i.e., a measure of randomness) derived from full (FP) and compact-pol (CP)

Table 2: Specification of the C-band full-pol RADARSAT-2 acquisitions over the test site during the field campaign (az: azimuth resolution and rg: range resolution)

Acquisition date	**Beam mode**	**Incidence angle range (deg.)**	**Orbit**	$az(\mathrm{m}) \times rg(\mathrm{m})$
05/07/2018	FQ15W	33.73–36.65	Ascending	4.73×5.11
29/07/2018	FQ15W	33.73–36.65	Ascending	4.73×5.11
22/08/2018	FQ15W	33.73–36.65	Ascending	4.73×5.11
09/10/2018	FQ15W	33.73–36.65	Ascending	4.73×5.11
02/11/2018	FQ15W	33.73–36.64	Ascending	4.73×5.11
26/11/2018	FQ15W	33.73–36.64	Ascending	4.73×5.11

SAR data.

4.1. Full-polarimetry

In FP SAR, the 2×2 complex scattering matrix $\mathbf{S}$ encompasses complete polarimetric information about backscattering from targets for each pixel. It is expressed in the backscatter alignment (BSA) convention in the linear horizontal (H) and linear vertical (V) polarization basis as,

$$\mathbf{S} = \begin{bmatrix} S_{\mathrm{HH}} & S_{\mathrm{HV}} \\ S_{\mathrm{VH}} & S_{\mathrm{VV}} \end{bmatrix} \tag{1}$$

Each element of the matrix represents the backscattering response of the target at a specific polarization. The diagonal elements of the matrix represent the co-polarized scattering information, while the off-diagonal terms represent the cross-pol information. In the monostatic backscattering case, the reciprocity theorem constrains the scattering matrix to be symmetric, *i.e.,* $S_{\mathrm{HV}} = S_{\mathrm{VH}}$.

To reduce the speckle effect in $\mathbf{S}$, the multi-looked Hermitian positive

semi-definite 3×3 coherency matrix $\mathbf{T}$ is obtained from the averaged outer product of the target vector $\boldsymbol{k}_P$ (derived using the Pauli basis matrix, Ψ_P) with its conjugate (Lee and Pottier, 2009).

$$\Psi_P = \left\{ \sqrt{2}\begin{bmatrix} 1 & 0 \\ 0 & 1 \end{bmatrix}, \sqrt{2}\begin{bmatrix} 1 & 0 \\ 0 & -1 \end{bmatrix}, \sqrt{2}\begin{bmatrix} 0 & 1 \\ 1 & 0 \end{bmatrix} \right\}$$

$$\boldsymbol{k}_P = \frac{1}{2}\mathrm{Tr}(\mathbf{S}\Psi_P) \implies \boldsymbol{k}_P = \frac{1}{\sqrt{2}}[S_{HH} + S_{VV}, S_{HH} - S_{VV}, 2S_{HV}]^T$$

$$\mathbf{T} = \frac{1}{N}\sum_{i=1}^{N} \boldsymbol{k}_{Pi}\boldsymbol{k}_{Pi}^{*T}$$

where N denotes the square window size for spatial averaging and Tr is the sum of the diagonal elements of the matrix.

When a polarized electromagnetic (EM) wave scatters from a random mixture of targets, it becomes partially polarized. The state of polarization of a partially polarized EM wave is characterized in terms of the degree of polarization ($0 \leq m \leq 1$). The degree of polarization is defined as the ratio of the (average) intensity of the polarized portion of the wave to that of the (average) total intensity of the wave. For a completely polarized EM wave, $m = 1$ and for a completely unpolarized EM wave, $m = 0$. In between these two extreme cases, the EM wave is said to be partially polarized, $0 < m < 1$.

Barakat (Barakat, 1977) provided an expression of m for the $N \times N$ coherency matrix. This expression is used in this study to obtain the degree of polarization m_{FP} from the 3×3 coherency matrix $\mathbf{T}$ for FP SAR data as,

$$m_{\mathrm{FP}} = \sqrt{1 - \frac{27|\mathbf{T}|}{\big(\mathrm{Tr}(\mathbf{T})\big)^3}}, \tag{2}$$

where $|\cdot|$ is the determinant of a matrix.

From the interpretation of the Huynen parameters in terms of certain general properties of the target geometry, it can be inferred that T_{11} is the generator of target symmetry and represents the scattered power from a regular, smooth and convex parts of the scatterer. Similarly, $(T_{22} + T_{33})$ is the generator of the target structure and represents the scattered power from an irregular, uneven and non-convex parts of the scatterer (Lee and Pottier, 2009). Therefore, with respect to the total polarized scattered power (i.e., $m_{\rm FP}$Span) from a scatterer, let us denote,

$$\tan\eta_1 = \frac{T_{11}}{m_{\rm FP}\,\text{Span}} \quad \text{and} \quad \tan\eta_2 = \frac{T_{22}+T_{33}}{m_{\rm FP}\,\text{Span}}, \tag{3}$$

where, $T_{11} = \langle|S_{\rm HH} + S_{\rm VV}|^2\rangle$, $T_{22} = \langle|S_{\rm HH} - S_{\rm VV}|^2\rangle$, and $T_{33} = 4\langle|S_{\rm HV}|^2\rangle$ are the diagonal elements of the $\mathbf{T}$ matrix with T_{11} and $T_{22} + T_{33}$ being roll-invariant quantities. The total power, Span is defined in terms of the elements of the $\mathbf{T}$ matrix as,

$$\text{Span} = T_{11} + T_{22} + T_{33}. \tag{4}$$

We define:

$$\tan\gamma_{\rm FP} = \tan\left(\eta_1 - \eta_2\right), \tag{5}$$

where $\gamma_{\rm FP}$ can be related to the average roll-invariant scattering-type parameter, Cloude $\overline{\alpha} \in [0°, 90°]$ (Cloude and Pottier, 1997). However, in order to compare the two parameters within the same range, they are suitably

modified as, $\widehat{\alpha} = 90^\circ - 2\overline{\alpha}$ and $\theta_{\mathrm{FP}} = 2\gamma_{\mathrm{FP}}$, which is given as,

$$\theta_{\mathrm{FP}} = 2\tan^{-1}\left(\frac{m_{\mathrm{FP}}\,\mathrm{Span}\,(T_{11} - T_{22} - T_{33})}{T_{11}\,(T_{22} + T_{33}) + m_{\mathrm{FP}}^2\,\mathrm{Span}^2}\right) \in [-90^\circ, 90^\circ]. \tag{6}$$

It can be noticed from equation (6) that when $T_{11} = 0$ and $m_{\mathrm{FP}} = 1$, then $\mathrm{Span} = T_{22} + T_{33}$ and $\theta_{\mathrm{FP}} = -90^\circ$. Similarly, when $T_{22} + T_{33} = 0$ and $m_{\mathrm{FP}} = 1$, then $\mathrm{Span} = T_{11}$ and $\theta_{\mathrm{FP}} = 90^\circ$. Besides, as θ_{FP} approaches 0, scattering randomness increases and at $\theta_{\mathrm{FP}} = 0^\circ$, the scattering is purely random (or depolarized).

The eigen-decomposition of $\mathbf{T}$ can be expressed as,

$$\mathbf{T} = \mathbf{U}_3\mathbf{\Sigma}\mathbf{U}_3^{-1} \tag{7}$$

where $\mathbf{\Sigma}$ is the 3×3 diagonal matrix with non-negative elements, $\lambda_1 \geq \lambda_2 \geq \lambda_3 \geq 0$, which are the eigenvalues of $\mathbf{T}$. The pseudo probabilities, p_i obtained from the eigenvalues are defined as,

$$p_i = \frac{\lambda_i}{\sum_{k=1}^{3}\lambda_k}, \tag{8}$$

which are then used to define the scattering entropy (Lee and Pottier, 2009) as,

$$H_{\mathrm{FP}} = -\sum_{k=1}^{3} p_k \log_3(p_k), \tag{9}$$

However, in this study, we use the quantity $\overline{H}_{\mathrm{FP}} = 1 - H_{\mathrm{FP}}$ to suitably represent the clusters in the $\overline{H}_{\mathrm{FP}}/\theta_{\mathrm{FP}}$ polar plane.

The feasible regions for $\overline{H}_{\mathrm{FP}}/\theta_{\mathrm{FP}}$ clustering plane can be represented by

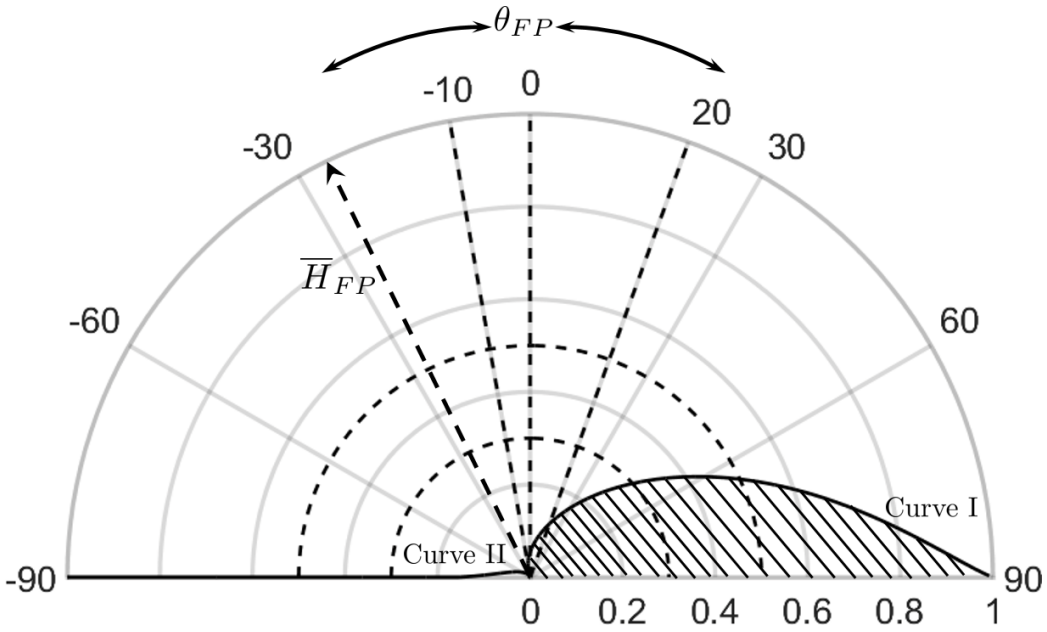

Figure 2: The $\overline{H}_{\mathrm{FP}}/\theta_{\mathrm{FP}}$ clustering plane displayed in polar plot. Curve I and Curve II represent the azimuthal symmetry lines. No scattering mechanisms exist in the dashed portion of the plane. Two half-circles at 0.5 and 0.7 divide the $\overline{H}_{FP}$ into high, medium and low entropy regions while $-90°$ to $-10°$ represents even bounce scattering, $-10°$ to $20°$ represents multiple bounce scattering and $20°$ to $90°$ represents odd bounce scattering.

two bounding curves, Curve I and Curve II as shown in Figure 2.

$$\text{Curve I}, [\mathbf{T}]_I = \begin{bmatrix} 1 & 0 & 0 \\ 0 & m & 0 \\ 0 & 0 & m \end{bmatrix} \quad 0 \leq m \leq 1 \tag{10}$$

$$\text{Curve II}, [\mathbf{T}]_{II} = \begin{bmatrix} 2m-1 & 0 & 0 \\ 0 & 1 & 0 \\ 0 & 0 & 1 \end{bmatrix} \quad 0.5 \leq m \leq 1 \tag{11}$$

4.2. Compact-polarimetry

The CP mode measures a projection of the 2×2 complex scattering matrix $\mathbf{S}$ as,

$$\begin{aligned} \begin{bmatrix} E_{CH} \\ E_{CV} \end{bmatrix} &= \frac{1}{\sqrt{2}} \begin{bmatrix} S_{HH} & S_{HV} \\ S_{VH} & S_{VV} \end{bmatrix} \begin{bmatrix} 1 \\ \pm i \end{bmatrix} \\ &= \frac{1}{\sqrt{2}} \begin{bmatrix} S_{HH} \pm iS_{HV} \\ S_{VH} \pm iS_{VV} \end{bmatrix} \end{aligned} \tag{12}$$

where the subscript C can be either the left-hand circular (L) transmit with a $+$ sign or the right-hand circular (R) transmit with a $-$ sign. The 2×2 covariance matrix is then obtained from the elements of the scattering vector as,

$$\mathbf{C}_2 = \begin{bmatrix} \langle |E_{CH}|^2 \rangle & \langle E_{CH} E_{CV}^* \rangle \\ \langle E_{CV} E_{CH}^* \rangle & \langle |E_{CV}|^2 \rangle \end{bmatrix}. \tag{13}$$

For CP-SAR data, the 4×1 Stokes vector $\vec{\mathbf{g}}$ can be written in terms of the elements of the 2×2 covariance matrix $\mathbf{C}_2$ as,

$$\vec{\mathbf{g}} = \begin{bmatrix} g_0 \\ g_1 \\ g_2 \\ g_3 \end{bmatrix} = \begin{bmatrix} C_{11} + C_{22} \\ C_{11} - C_{22} \\ C_{12} + C_{21} \\ \pm j\,(C_{12} - C_{21}) \end{bmatrix}, \tag{14}$$

where $\pm$ corresponds to left and right circular polarization respectively.

From the elements of $\vec{\mathbf{g}}$, the backscatter power in the same sense ($SC = \frac{g_0 - g_3}{2}$) and opposite sense ($OC = \frac{g_0 + g_3}{2}$) to the transmitted circular polariza-

tion is utilized to derive the roll-invariant scattering-type parameter (θ_{CP}) for the compact-polarimetric SAR data similar to the FP case. Here, OC is the generator of target symmetry and represents the scattered power from a regular, smooth and convex parts of the scatterer. Similarly, SC is the generator of the target structure and represents the scattered power from an irregular, uneven and non-convex parts of the scatterer:

$$\tan\zeta_1 = \frac{OC}{m_{\mathrm{CP}}\,\mathrm{Span}}, \quad \text{and} \quad \tan\zeta_2 = \frac{SC}{m_{\mathrm{CP}}\,\mathrm{Span}} \tag{15}$$

where the total power Span is defined as,

$$\mathrm{Span} = SC + OC \tag{16}$$

Similar to FP, we define:

$$\tan\gamma_{\mathrm{CP}} = \tan\left(\zeta_1 - \zeta_2\right) \tag{17}$$

where γ_{CP} can be analogously related to the polarization ellipticity parameter $\chi \in [-45^\circ, 45^\circ]$. However, in order to compare, the two parameters within the same range, they are suitably scaled as, $\overline{\chi} = -2\chi$ and $\theta_{\mathrm{CP}} = 2\gamma_{\mathrm{CP}}$ which is given as,

$$\theta_{\mathrm{CP}} = 2\tan^{-1}\left(\frac{m_{\mathrm{CP}}\,\mathrm{Span}\,(OC - SC)}{OC \times SC + m_{\mathrm{CP}}^2\,\mathrm{Span}^2}\right) \in [-90^\circ, 90^\circ] \tag{18}$$

Similar to θ_{FP}, it can be noticed from (18) that for a pure dihedral scatterer, i.e., when $OC = 0$ and $m_{\mathrm{CP}} = 1$, then $\mathrm{Span} = SC$ and $\theta_{\mathrm{CP}} = -90^\circ$. Similarly, for a pure trihedral scatterer, i.e., when $SC = 0$ and $m_{\mathrm{CP}} = 1$,

then Span $= OC$ and $\theta_{\mathrm{CP}} = 90°$. Besides, as θ_{CP} approaches 0, scattering randomness increases and at $\theta_{\mathrm{CP}} = 0°$, the scattering is purely random (or depolarized).

The expression for the Barakat degree of polarization for the compact-polarimetric case is given as,

$$m_{\mathrm{CP}} = \sqrt{1 - \frac{4|\mathbf{C}_2|}{\left(\mathrm{Tr}(\mathbf{C}_2)\right)^2}}. \tag{19}$$

The eigen-decomposition of $\mathbf{C}_2$ can be expressed as,

$$\mathbf{C}_2 = \mathbf{U}_2 \mathbf{\Sigma} \mathbf{U}_2^{-1}, \tag{20}$$

where $\mathbf{\Sigma}$ is a 2×2 diagonal matrix with non-negetive elements, $\lambda_1 \geq \lambda_2 \geq 0$, which are the eigenvalues of $\mathbf{C}_2$. The pseudo probabilities, p_i obtained from the eigenvalues are defined as,

$$p_i = \frac{\lambda_i}{\sum_{k=1}^{2} \lambda_k}, \tag{21}$$

which are then used to define the scattering entropy (H_{CP}) for CP-SAR data as,

$$H_{\mathrm{CP}} = -\sum_{k=1}^{2} p_k \log_2 (p_k). \tag{22}$$

As mentioned earlier for the FP case, we use the quantity $\overline{H}_{\mathrm{CP}} = 1 - H_{\mathrm{CP}}$ to suitably represent the clusters in the $\overline{H}_{\mathrm{CP}}/\theta_{\mathrm{CP}}$ polar plane.

Similar to FP, the feasible regions for $\overline{H}_{\mathrm{CP}}/\theta_{\mathrm{CP}}$ clustering plane can be represented by two bounding curves, Curve I and Curve II, as shown in

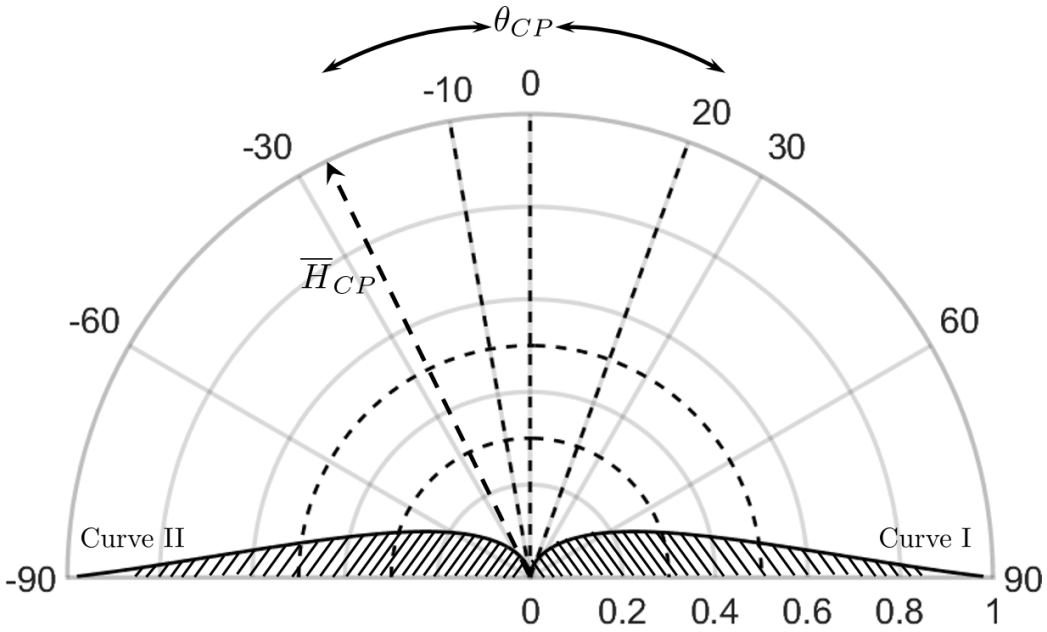

Figure 3: The $\overline{H}_{\mathrm{CP}}/\theta_{\mathrm{CP}}$ clustering plane displayed in polar plot. Curve I and Curve II represent the azimuthal symmetry lines. No scattering mechanisms exist in the dashed portion of the plane. Two half-circles at 0.5 and 0.7 divide the $\overline{H}_{CP}$ into high, medium and low entropy regions while $-90°$ to $-10°$ represents even bounce scattering, $-10°$ to $20°$ represents multiple bounce scattering and $20°$ to $90°$ represents odd bounce scattering.

Figure 3.

$$\text{Curve I}, [\mathbf{C}]_I = \begin{bmatrix} \frac{2m+1}{4} & i\frac{2m-1}{4} \\ -i\frac{2m-1}{4} & \frac{2m+1}{4} \end{bmatrix} \quad 0 \leq m \leq 0.5 \tag{23}$$

$$\text{Curve II}, [\mathbf{C}]_{II} = \begin{bmatrix} \frac{2m+1}{4} & -i\frac{2m-1}{4} \\ i\frac{2m-1}{4} & \frac{2m+1}{4} \end{bmatrix} \quad 0 \leq m \leq 0.5 \tag{24}$$

4.3. Clustering

Cloude and Pottier (Cloude and Pottier, 1997) proposed a clustering scheme $H/\overline{\alpha}$, for FP SAR data based on the average scattering-type parameter ($\overline{\alpha}$) and the scattering entropy (H). The $H/\overline{\alpha}$ plane is sub-divided

into nine zones to suitably cluster various scattering mechanisms. The properties of different scattering mechanisms determine the boundaries between the zones. Hence certain assumptions are utilized in the proper setting of these boundaries. Subsequently, the 2D clustering plane is extended to 3D $H/A/\overline{\alpha}$ space by introducing the scattering anisotropy parameter A. This parameter, which is complementary to H, is useful to discriminate targets when $H > 0.7$. However, for lower values of H, this parameter is noisy and could introduce inaccuracies in determining the clusters. In the literature, this clustering scheme is extended for dual-pol SAR data (HH-HV or VV-VH) by suitably modifying the zone boundaries (Ji and Wu, 2015).

In our study, we propose a clustering scheme equivalently for both FP and CP SAR data by utilizing the 2D $\overline{H}_{\mathrm{FP}}/\theta_{\mathrm{FP}}$ and $\overline{H}_{\mathrm{CP}}/\theta_{\mathrm{CP}}$ planes respectively. Besides, the zones and the boundaries of both the clustering planes are identical. From analysis with scattering model (random volume model), it has been observed that the scattering-type from vegetation lies approximately in the range -10° to 20° (Antropov et al., 2011). The upper bound for multiple scattering ($\theta_X = 20^{\circ}$) is characterized by equal contributions from the ensemble of horizontal and vertical dipole scattering components from vegetation structure. In contrast, the lower bound ($\theta_X = -10^{\circ}$) is the characteristic of multiple scattering phenomena predominantly described by vertical vegetation structure. Hence, this region is subdivided for multiple scattering mechanisms. Unlike the $H/\overline{\alpha}$ plane, the proposed clustering scheme divides the plane into twelve zones. The scattering-type parameter θ_X (where X refers to both FP and CP) divides the $\overline{H}_X - \theta_X$ plane into four sub-planes (P1:(Z1, Z2, Z3); P2:(Z4, Z5, Z6); P3:(Z7, Z8, Z9); P4:(Z10, Z11,

Z12)) which consists of (1) pure even-bounce scattering ($-90°$ to $-10°$) in P1; (2) even-bounce with multiple scattering ($-10°$ to $0°$) in P2; (3) odd-bounce with multiple scattering ($0°$ to $20°$) in P3; (4) pure odd-bounce scattering ($20°$ to $90°$) in P4. The quantity $\overline{H}_X = 1 - H$ divides the plane into (1) high entropy (0 to 0.3); (2) medium entropy (0.3 to 0.5); (3) low entropy (0.5 to 1). The $H/\overline{\alpha}$ and the $\overline{H}_X/\theta_X$ clustering plane along with the zones are given in Figure 4.

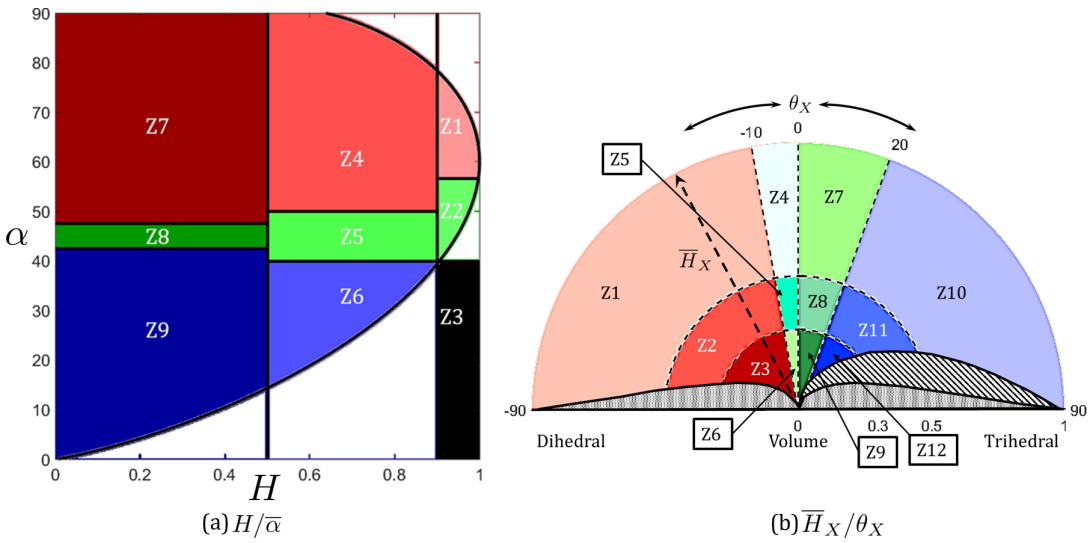

Figure 4: (a) $H/\overline{\alpha}$ clustering plane for FP SAR data and (b) $\overline{H}_X/\theta_X$ plane for both FP and CP SAR data.

The difference between the geometrical structures of the $H/\overline{\alpha}$ and $\overline{H}_{\mathrm{FP}}/\theta_{\mathrm{FP}}$ 2D clustering planes can be observed in Figure 4. As stated earlier, it may be noted that the parameter $\overline{\alpha}$ is scaled to $\widehat{\alpha} = 90° - 2\overline{\alpha}$ solely for the sake of qualitative comparison. The ability of the two clustering planes, i.e., $\overline{H}_{\mathrm{FP}}/\theta_{\mathrm{FP}}$ and $\overline{H}_{\mathrm{CP}}/\theta_{\mathrm{CP}}$ to classify different landcover classes is apparent in this figure. Region A, B and C in Figure 5 are respectively the oriented urban area, forest area and ocean areas. The dashed white box in Figure 5

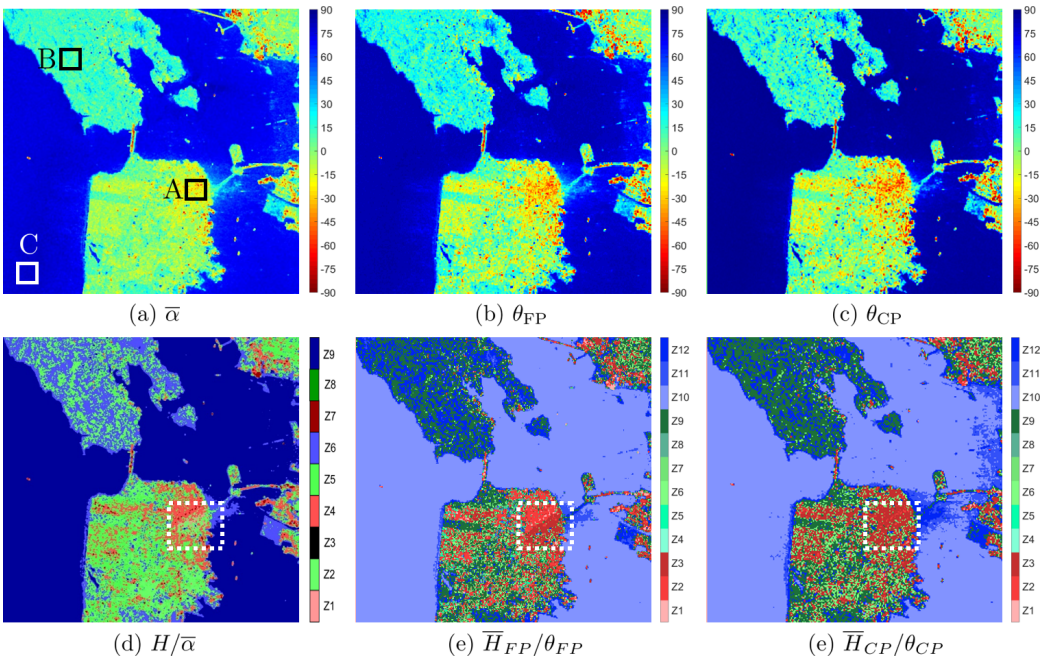

(a) $\overline{\alpha}$ (b) θ_{FP} (c) θ_{CP}

(d) $H/\overline{\alpha}$ (e) $\overline{H}_{FP}/\theta_{FP}$ (e) $\overline{H}_{CP}/\theta_{CP}$

Figure 5: The scattering type parameters, $\overline{\alpha}$, θ_{FP}, θ_{CP} and the $H/\overline{\alpha}$, $\overline{H}_{\mathrm{FP}}/\theta_{\mathrm{FP}}$, $\overline{H}_{\mathrm{CP}}/\theta_{\mathrm{CP}}$ clustered image of San Francisco Bay, USA using C-band RS-2 SAR data. Region A represents the oriented urban area, region B and C represents forest and ocean areas, respectively. The white box shows the oriented urban area where the major change during clustering occured. $H/\overline{\alpha}$ identified it as scattering from vegetation while $\overline{H}_{\mathrm{FP}}/\theta_{\mathrm{FP}}$ and $\overline{H}_{\mathrm{CP}}/\theta_{\mathrm{CP}}$ correctly identified it as scattering from urban region.

highlights distinct changes in the scattering types as well as the clustering zones for differently oriented targets.

It can be observed from Figure 6 that in the $H/\overline{\alpha}$ plane, the even-bounce scattering mechanism over oriented urban area (A) is only 17 % while the odd-bounce and multiple-bounce scattering mechanism are 38 % and 45 %, respectively. In contrast, the contribution of even-bounce dominant scattering mechanism in $\overline{H}_{\mathrm{FP}}/\theta_{\mathrm{FP}}$ and $\overline{H}_{\mathrm{CP}}/\theta_{\mathrm{CP}}$ are 84 % and 79 %, respectively. On the other hand, over the forest area (B), the multiple-bounce scattering mechanism is 8 % higher for $\overline{H}_{\mathrm{FP}}/\theta_{\mathrm{FP}}$ and 6 % higher for $\overline{H}_{\mathrm{CP}}/\theta_{\mathrm{CP}}$ as compared

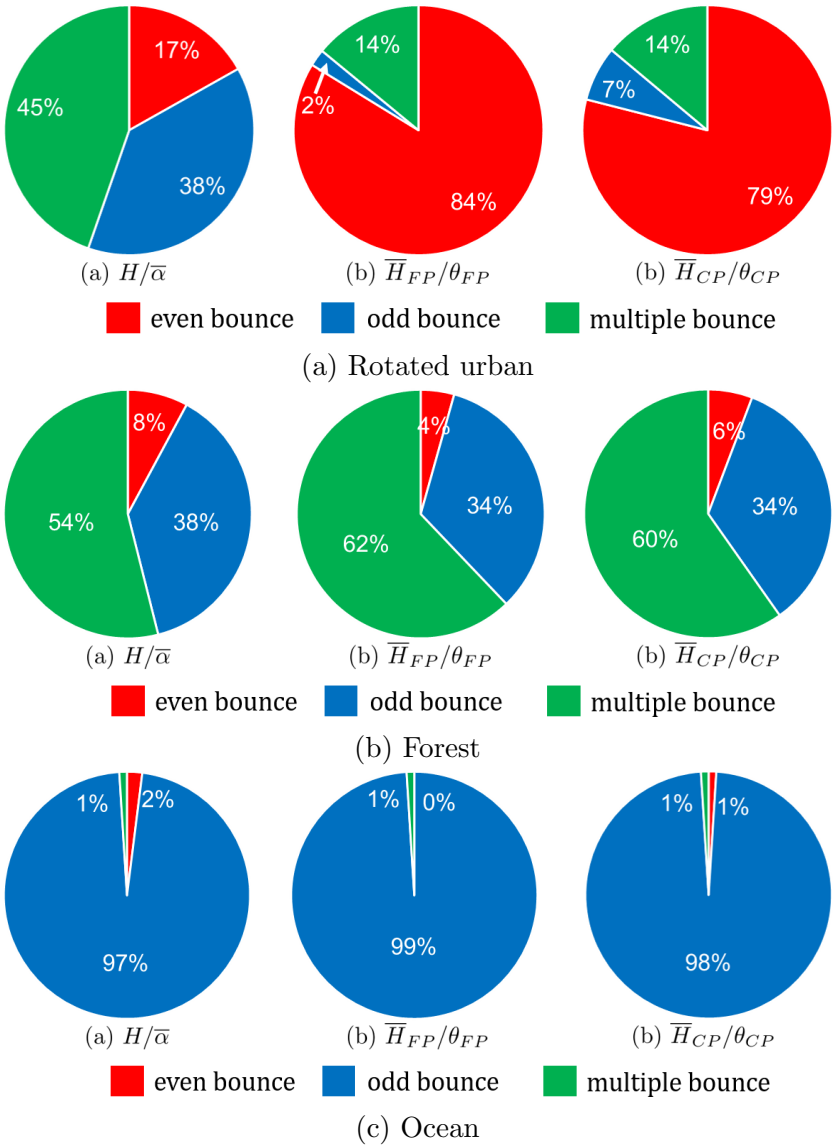

Figure 6: A comparison of the percentages of even, odd and multiple bounce scattering over (a) rotated urban, (b) forest and (c) ocean surfaces for the C-band RS-2 San Francisco Bay area image using $H/\overline{\alpha}$, $\overline{H}_{\rm FP}/\theta_{\rm FP}$ and $\overline{H}_{\rm CP}/\theta_{\rm CP}$ clustering techniques.

to $H/\overline{\alpha}$. Similarly, over the ocean area (C) the odd-bounce scattering mechanism has increased marginally by 2 % and 1 % for $\overline{H}_{\rm FP}/\theta_{\rm FP}$ and $\overline{H}_{\rm CP}/\theta_{\rm CP}$,

respectively. This suggests that the discriminating ability of $\overline{H}_{\mathrm{FP}}/\theta_{\mathrm{FP}}$ and $\overline{H}_{\mathrm{CP}}/\theta_{\mathrm{CP}}$ scheme is by and large higher than $H/\overline{\alpha}$. This marked ability might be due to 1) the joint utilization of the Barakat degree of polarization along with essential information from elements of the coherency matrix in deriving the scattering-type parameters, 2) the notion of an extended clustering procedure (i.e., 12 clusters) using entropy and the scattering-type parameters. Hence, we use the proposed clustering schemes with θ_{FP} and θ_{CP}, for the temporal analysis of two different varieties of rice crops over Vijayawada, India using FP RADARSAT-2 data and simulated CP SAR data. In this study, we analyze the phenological changes of rice using these parameters and the new clustering scheme.

5. Results and Discussion

The study area in Vijayawada is well facilitated with water for crop cultivation throughout the year. The temporal analysis of θ_{FP} and θ_{CP} along with $\overline{H}_{\mathrm{FP}}/\theta_{\mathrm{FP}}$ and $\overline{H}_{\mathrm{CP}}/\theta_{\mathrm{CP}}$ clustering plane for rice will be discussed in this section.

5.1. Temporal variation of θ_{FP} and θ_{CP} for FP and CP data

The temporal variation of θ_{FP} and θ_{CP} for FP and CP SAR data, respectively, are shown in Figure 7. As stated earlier, for any deterministic target, θ_{FP} and θ_{CP} lie at the extremities of the range, i.e., -90° to 90°. For both θ_{FP} and θ_{CP}, -90° indicates pure dihedral scattering, while 90° indicates pure trihedral scattering. For pure diffused scattering, θ_{FP} and $\theta_{\mathrm{CP}} \approx 0^\circ$. However, for any other distributed targets, θ_{FP} and θ_{CP} varies within these limits.

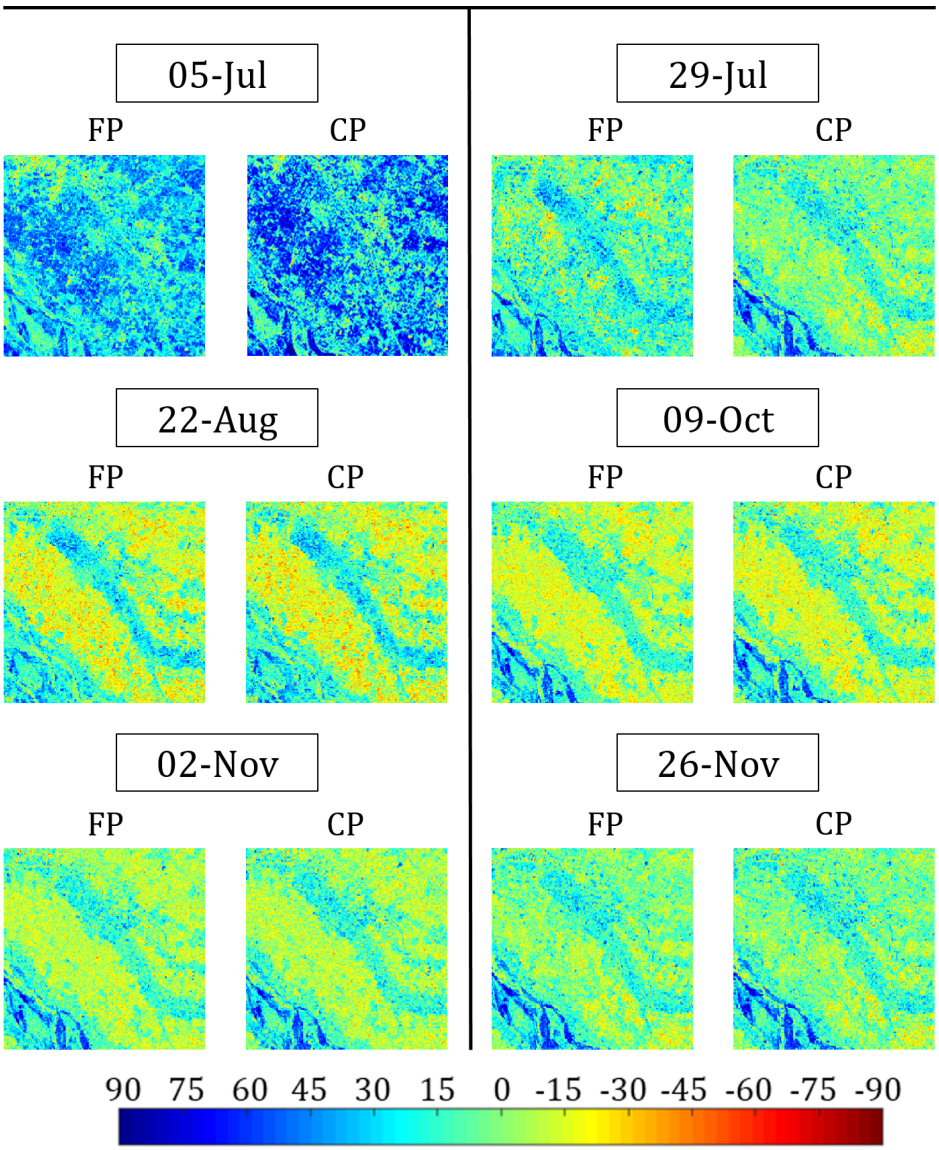

Figure 7: Variation of θ_{FP} and θ_{CP} images for FP and CP over the study area. The growth stages are: 5-Jul: Bare field, 29-Jul: Early tillering, 22-Aug: Advanced tillering, 9-Oct: Flowering, 2-Nov: Early dough, and 26-Nov: Maturity

386 During the first week of July, there was no crop in most of the rice fields.

387 Hence, the SAR response was primarily dominated by the soil character-

istics in this period. On 29 Jul, a significant difference in θ_{FP} values can be observed in those fields. In that particular area, transplantation of rice was mostly completed, while certain fields entered the early tillering stage. Hence, majority of the rice fields showed even-bounce multiple scattering with θ_{FP} varies from 0° to -20°. Additionally, the rice fields, which were at the end of the tillering stage, showed moderate even-bounce scattering with θ_{FP} varies from -30° to -50°.

On 22 Aug, most of the rice fields were at the advanced tillering stage. Therefore, high even-bounce multiple scattering is prominent in these fields. Around 09 Oct, rice fields reached the end of the vegetative stage, and thus θ_{FP} for the area showed even-bounce multiple scattering mechanisms. On 26 Nov, rice reached the maturity stage. At this time, crop water content got reduced, and the canopy geometry appeared complex due to the randomly oriented stem with grains that are evident from in-situ measurements. Thus, this complex structure generated a random-volume scattering mechanism from most of the fields in that area.

Similarly, θ_{CP} shows changes from high odd-bounce to even-bounce multiple scattering within the growing season of rice. However, few minor differences in the response of θ_{CP} from θ_{FP} can be noticed mainly during the higher phenological growth stages. These differences might be due to the formulation of the compact polarimetric Stokes vector that is obtained from the projection of the scattering matrix with reduced polarimetric information. Due to this reason, for high cross-pol components, the difference between SC and OC powers becomes negligible, and θ_{CP} exhibits high diffused scattering. As stated earlier, on 5 Jul, most of the fields were empty. Hence, like θ_{FP},

θ_{CP} also exhibits a high amount of odd-bounce scattering in those fields.

On 29 Jul, a notable change in the response of θ_{FP} and θ_{CP} for a few fields must be due to different sowing date. During this period, rice was transplanted and progressed to the early tillering stage, which shows dominant even-bounce multiple scattering. From 09 Oct to 26 Nov, dominant even-bounce multiple scattering is evident due to numerous branch and foliage development with an increase in the plant area index. However, the range of θ_{CP} for even-bounce multiple scattering is higher than θ_{FP}. This high value of θ_{CP} might be because of the high cross-pol component due to which the difference between SC and OC power is almost negligible. For the quantitative temporal analysis of θ_{FP} and θ_{CP}, five different field points were selected from the fields.

In this study, both qualitative and quantitative analyses of the temporal variations in θ_{FP} and θ_{CP} utilizing data from five in-situ points (viz., P012, P054, P064, P034, P053) are shown in Figure 8. The values of θ_{FP} and θ_{CP} on 05 Jul indicate dominant odd-bounce scattering from bare soil. However, on 29 Jul, a sudden change in θ_{FP} and θ_{CP} values are noticed. During this period, θ_{FP} ranges from -17° to -51° while θ_{CP} ranges from -23° to -62°. These sudden changes in the values of θ_{FP} and θ_{CP} are due to the early tillering stage of rice. At this point, the soil was highly saturated, and the vertical stems acted like a dihedral scatterer which leads to even-bounce scattering from the rice fields. A similar response of rice during the tillering phase was also reported by Lopez-Sanchez et al. (2014).

Contrarily, we observe an increasing trend in the plots between 22 Aug and 2 Nov due to the reduction in even-bounce multiple scattering. During

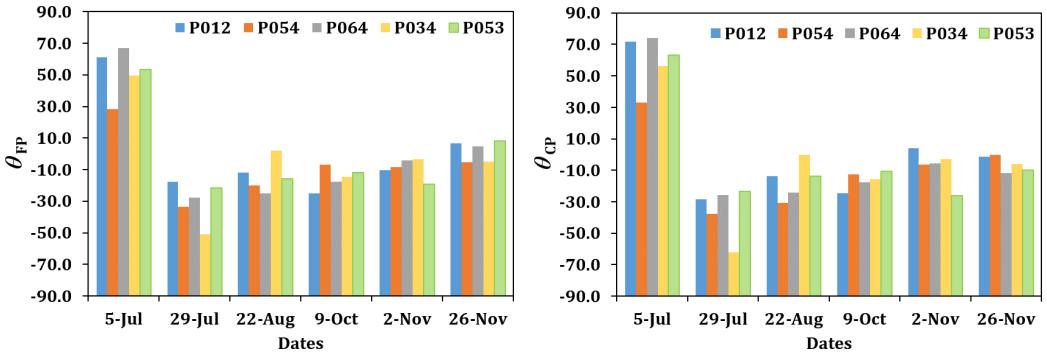

(a) FP (b) CP

Figure 8: Temporal variation of θ_{FP} and θ_{CP} for rice using FP and CP data. The growth stages are: 5-Jul: Bare field, 29-Jul: Early tillering, 22-Aug: Advanced tillering, 9-Oct: Flowering, 2-Nov: Early dough, and 26-Nov: Maturity

this time, rice advanced from advance tillering to early dough stage, and hence, we observe increased multiple scattering from these fields. Therefore, the coherence between the co-polarized channels decreased significantly. The range of θ_{FP} value during this period was 2° to -25° and θ_{CP} value was 0° to -30°. However, towards the end of the season, randomness in θ_{FP} and θ_{CP} values are observed due to complex scattering from the rice stem and grains.

5.2. $\overline{H}_{FP}/\theta_{FP}$ and $\overline{H}_{CP}/\theta_{CP}$ clustering planes for rice

As discussed earlier, the $\overline{H}_{\mathrm{FP}}/\theta_{\mathrm{FP}}$ and $\overline{H}_{\mathrm{CP}}/\theta_{\mathrm{CP}}$ planes are divided into 12 zones based on different scattering-type information. In this study, these clustering zones (Figure 11) are utilized to monitor the growth stages of rice using full (Figure 9) and simulated compact (Figure 10) polartimetric SAR data.

In Figure 9 and Figure 10, the θ_{FP} and θ_{CP} values are majorly within the odd-bounce scattering region on 05 Jul due to the nearly smooth soil surface condition. Hence, dense clusters are seen in Z10, Z11, and Z12, which corre-

sponds respectively to low entropy even-bounce scattering, medium entropy even-bounce scattering, and high entropy even-bounce scattering regions. Moreover, a few data points lying in region Z3 is due to the early transplantation stage. Besides, tillage operation in some fields has produced soil surface roughness, which increased the entropy, and hence, a sparse cluster can also be seen in Z9 and Z6. The proportion of pixels over different scattering regions at each phenological stage is shown in Table 3. To characterize different changes in scattering mechanisms, we have considered (Z1, Z2, Z3) as even bounce scattering, (Z10, Z11, Z12) as odd bounce scattering and (Z4, Z5, Z6, Z7, Z8, Z9) as multiple bounce scattering. High odd bounce scattering (86.26 %) was noted for FP data. Besides, due to the slight roughness a small component of multiple bounce scattering (12.24 %) is observed during this period, whereas even bounce scattering contribution was only 0.90 %.

A significant change in the data cluster is seen on 29 Jul. During this period, most of the rice fields were in the early tillering stage, while other non-cultivated fields had moist soil with high roughness that is evident from in-situ data. This highly rough soil surface during this period has generated a high degree of randomness in the received EM wave, which resulted in an increased entropy. Hence, a shift from low entropy zone (Z10) to high (Z12) and medium (Z11) entropy zones is evident on 29 Jul. Also, some data points in zones Z11 and Z12 are $\theta_{\mathrm{FP}} \leq 30^{\circ}$, which is due to the scattering from the water surface in the rice fields (Lopez-Sanchez et al., 2014). However, compared to θ_{FP}, the values of θ_{CP} are 5° to 10° higher in this period.

The density of the data points in Z6 and Z9 zones has also increased on 29 Jul, while rice transplantation was undergoing in some other fields.

Therefore, a moderately high accumulation of data points can also be seen in Z3 (Figure 9 and Figure 10). Moreover, the previously sown rice fields had achieved a higher vegetative stage due to which the areal coverage by the crop canopy had increased, thereby slightly decreasing the scattering entropy. Due to this aspect, a few data points are sparsely clustered in the Z2 region on 29 Jul. Furthermore, in zones Z2 and Z3, the values of θ_{CP} is 2° to 5° higher than θ_{FP}. Hence, the even bounce scattering had increased by 75.89 % and multiple scattering had increased by 16.49 %. A noteworthy decrease in the odd bounce scattering (82.38 %) is observed which is most likely due to the increase of double-bounce for the presence of stems, which also helps to reduce the surface roughness and the contribution from the ground.

On 22 Aug, dense clusters can be seen in Z3 for FP and CP data, which is due to the tillering stage of rice. During this stage, the fields are flooded with water, and the stems are almost vertical, which acts as dihedral scatterers. During this period, $\overline{H}_{\mathrm{CP}}$ is lower than $\overline{H}_{\mathrm{FP}}$, which might be due to less polarimetric information content. Similar to 29 Jul, θ_{CP} is higher than θ_{FP} at this time. Additionally, due to the variation in the θ_{CP} and H_{CP} values according to crop morphology, significant change among Z5, Z6, Z8, and Z9 zones can be observed compared to 29 Jul. Moreover, in $\overline{H}_{\mathrm{FP}}/\theta_{\mathrm{FP}}$ plot, cluster formation in Z5 and Z8 zones is seen, whereas, in $\overline{H}_{\mathrm{CP}}/\theta_{\mathrm{CP}}$ plot, no such clusters are found due to the high entropy in the CP SAR data.

In general, the occurrence of flooding in rice fields generates even-bounce scattering (Yonezawa et al., 2012). Hence, a significant shift in the scattering mechanism from odd-bounce to even-bounce is visible during 22 Aug.

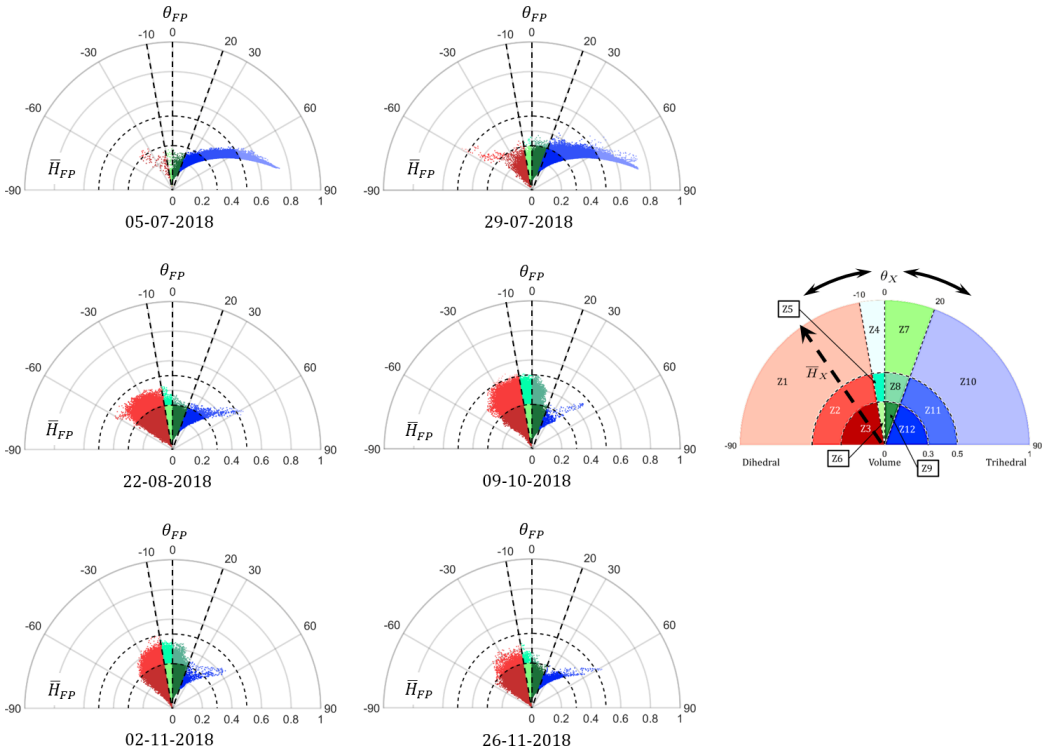

Figure 9: The $\overline{H}_{\mathrm{FP}}/\theta_{\mathrm{FP}}$ scatter plane for rice fields using FP SAR data. The growth stages are: 5-Jul: Bare field, 29-Jul: Early tillering, 22-Aug: Advanced tillering, 9-Oct: Flowering, 2-Nov: Early dough, and 26-Nov: Maturity

However, the orientation, shape, and size of each crop were not the same, and hence there was also a possibility of rough soil surface stretching out from the water surface. Therefore, these phenomena could induce high randomness in the scattered EM wave. Besides, similar to 29 Jul, some fields progressed to a higher vegetative stage due to which a cluster can be seen in Z2. Furthermore, fields that reached the booting stage display even-bounce multiple scattering with medium entropy characteristics (Z5). However, the even-bounce scattering mechanism is evident throughout the tillering stage. Hence, the even bounce scattering power had decreased by 11.19 %, while

multiple bounce scattering had marginally increased by 3.67 %.

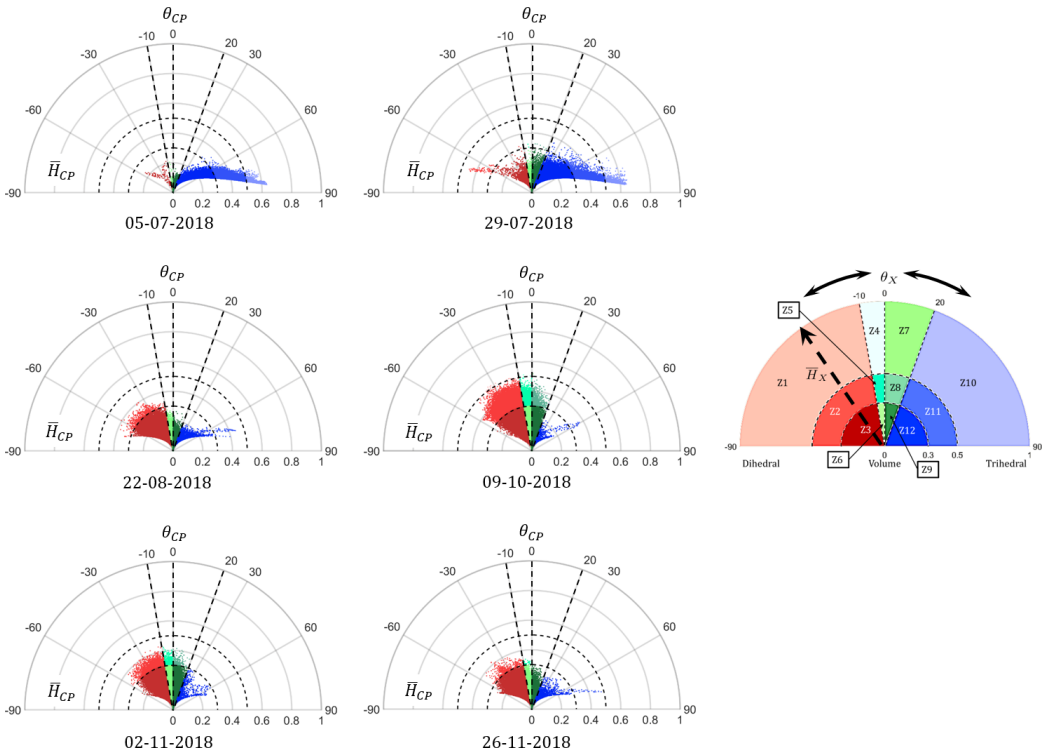

Figure 10: The $\overline{H}_{\mathrm{CP}}/\theta_{\mathrm{CP}}$ scatter plane for rice fields using simulated CP SAR data. The growth stages are: 5-Jul: Bare field, 29-Jul: Early tillering, 22-Aug: Advanced tillering, 9-Oct: Flowering, 2-Nov: Early dough, and 26-Nov: Maturity

On 09 Oct, both $\overline{H}_{\mathrm{FP}}/\theta_{\mathrm{FP}}$ and $\overline{H}_{\mathrm{CP}}/\theta_{\mathrm{CP}}$ planes show a shift towards the medium entropy region (i.e., Z2 and Z5 zones) which is evident in Figure 9. During this period, most of the rice fields were in the inflorescence emergence stage, with θ_{FP} and θ_{CP} indicating even-bounce and even-bounce multiple scatterings. Moreover, the amount of cross-pol components has increased during this period. A similar type of increase in cross-pol components from transplantation to maturity stages was reported by He et al. (2018). The shift towards the Z2 and Z5 zones indicates an even-bounce scattering mechanism

of the scattered EM wave. Such a response might be due to the extinction of the vertical polarization due to the canopy structure. Also, the amount of odd-bounce scattering reduced during this period, and rice foliage generated moderate odd-bounce multiple scattering due to which dense cluster in the Z8 zone is noticed in Figure 9 and Figure 10. The contribution of multiple bounce scattering was 40.02 % due to the full-grown rice crop with differently oriented stem, leaf structures and flowers.

Around 02 Nov, the rice fields reached the early dough stage, during which, the milky white substance begins to accumulate in rice panicle. Simultaneously, the crop water content during this period remains very high, while leaf and stem produce overall complex canopy structure, which leads to high randomness in the SAR backscatter. Due to this fact, the values of $\overline{H}_{\mathrm{FP}}$ and $\overline{H}_{\mathrm{CP}}$ are low, which is apparent in Z2, Z5, and Z8 zones. Moreover, at this point, the clusters in Z3 and Z2 zones are due to the scattering from compound leaf and stem structure. In contrast, clusters in Z6, Z5, Z8, and Z9 zones are due to multiple scattering contribution from the intermediate complex rice canopy layer. The cluster in the Z12 zone corresponds to the scattering of the wave directly from the leaves of the uppermost canopy layer. During this time further decrease in even bounce scattering is evident.

On 26 Nov, the rice fields reached the maturity stage, and the grains become firm and heavy. At this point, the crop becomes dry, whereas the moisture content in grains remains $\approx$20 %. Due to the weight of the grains, lodging of rice is usually visible in the fields due to which the morphological condition becomes further complicated than the dough stage. Hence, an additional increase in the scattering entropy during this period is apparent

for both FP and CP SAR data. High densities of clusters in Z3, Z6, Z9, and Z12 zones can be noticed, which is due to scattering from the complex geometrical structure of rice at this stage. However, a small cluster can also be observed in the Z11 zone, which might be due to fully or partially harvested rice fields. At this stage, the highest contribution of multiple scattering mechanisms (73.23 %) is profound due to the increase in scattering randomness within the SAR resolution cell.

Table 3: Changes in the scattering mechanisms across different dates and between FP and CP data. we have considered (Z1, Z2, Z3) as even bounce scattering, (Z10, Z11, Z12) as odd bounce scattering and (Z4, Z5, Z6, Z7, Z8, Z9) as multiple bounce scattering. The dominant scattering mechanism(s) at each date is highlighted in bold font.

Dates	**Modes**	**Even bounce scattering**	**Odd bounce scattering**	**Multiple bounce scattering**	**Growth Stage**
05/07/2018	FP	0.90%	**86.86%**	12.24%	Bare field
	CP	0.60%	**88.28%**	11.12%	
29/07/2018	FP	**76.79%**	4.48%	28.73%	Early tillering
	CP	**64.60%**	2.10%	33.30%	
22/08/2018	FP	**65.60%**	2%	32.40%	Advanced tillering
	CP	**63.87%**	2%	34.13%	
09/10/2018	FP	**58.10%**	1.88%	**40.02%**	Flowering
	CP	**56.33%**	1.88%	**41.79%**	
02/11/2018	FP	39.40%	3%	**57.60%**	Early dough
	CP	31.60%	2%	**66.40%**	
26/11/2018	FP	25.61%	1.16%	**73.23%**	Maturity
	CP	16.76%	0.92%	**82.30%**	

It is noteworthy that the differences in the characterization capability between FP and CP SAR data depends on the type and geometry of the targets. Moreover, the spatial heterogeneity induces the changes in the intensity of the co-pol and cross-pol components. Hence, a change in the scattered EM wave is sometimes evident between FP and CP SAR data.

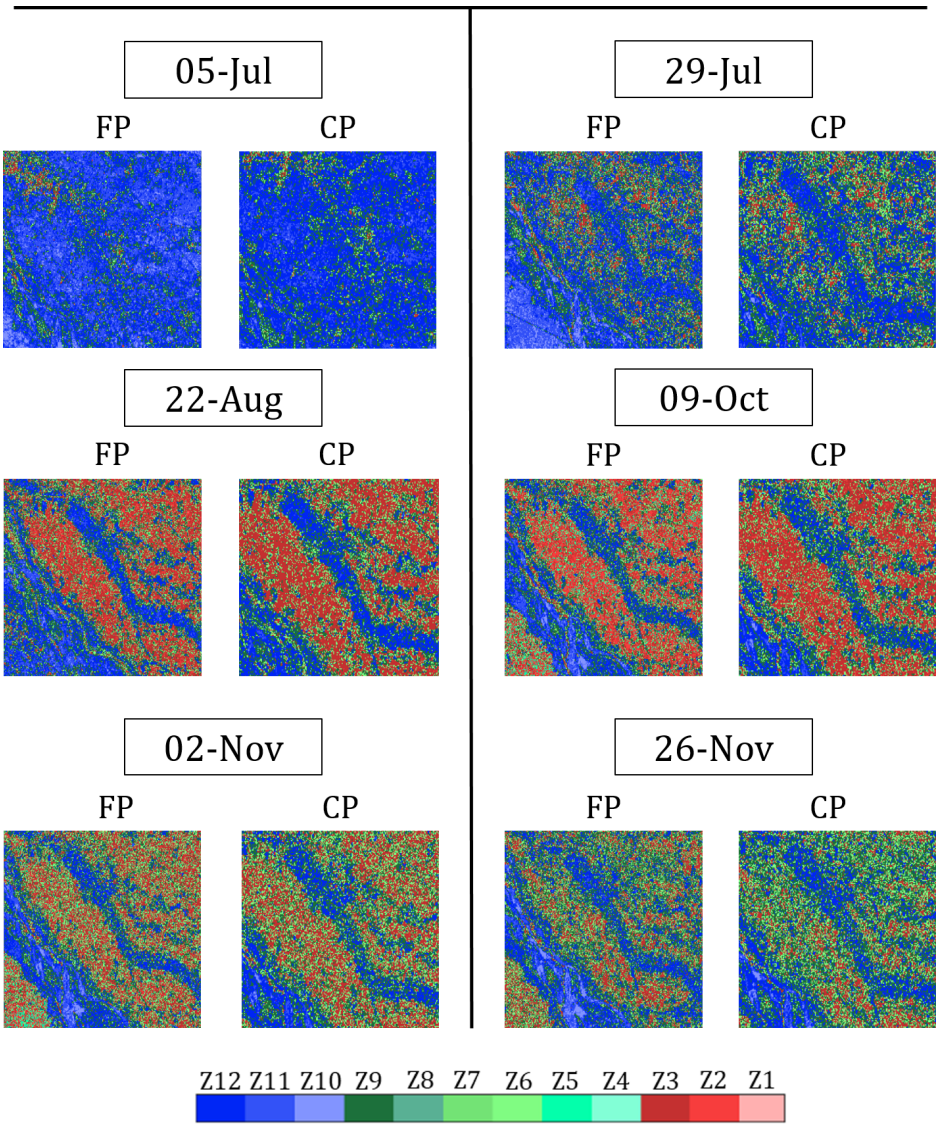

Figure 11: Variation of $\overline{H}_{\mathrm{FP}}/\theta_{\mathrm{FP}}$ and $\overline{H}_{\mathrm{CP}}/\theta_{\mathrm{CP}}$ clustered images for FP and CP over the study area. The growth stages are: 5-Jul: Bare field, 29-Jul: Early tillering, 22-Aug: Advanced tillering, 9-Oct: Flowering, 2-Nov: Early dough, and 26-Nov: Maturity

6. Conclusions

In this study, we have proposed two scattering-type parameters, θ_{FP} and θ_{CP} for identifying target scattering mechanism for both full (FP) and com-

pact polarimetric (CP) SAR data. These quantities are roll-invariant and vary in the range, -90° to 90°. In particular these two scattering-type parameters jointly utilize the received antenna basis-invariant parameters, i.e., the Barakat degree of polarization and the total scattering power (Span) and the elements of the coherency matrix. The two extreme values of their range correspond to even-bounce (-90°), and odd-bounce (90°) scattering mechanisms, while $\theta_{\mathrm{FP}} = 0$ and $\theta_{\mathrm{CP}} = 0$ denotes diffused scattering mechanism. Furthermore, θ_{FP} and θ_{CP} within the range, -10° to 0° indicates even-bounce multiple scattering components, and 0° to 20° denotes the odd-bounce multiple scattering components.

In this study, we have suitably fulfilled our primary objective to characterize changes in the scattering mechanism with the advancement of crop phenological stages. We have used the scattering-type parameters for the temporal analysis of rice over the Vijayawada test site in India using FP and CP SAR data. The sensitivities of θ_{FP} and θ_{CP} with growth stages of rice are significantly evident from this study.

During the initial period of the growing season, both θ_{FP} and θ_{CP} show odd-bounce scattering due to bare ground conditions. Subsequently, changes in the scattering-type from those fields were noticed depending on the sowing time, and morphological characteristics of rice. Changes in the scattering-type from odd-bounce to even-bounce at the beginning of the tillering stage from 29 Jul is adequately captured by θ_{FP}, and θ_{CP} values.

We observed the saturation in θ_{FP} and θ_{CP} values during the advanced reproductive stage, which was due to weak alteration of crop canopy geometry. Later, close to the senescence stage, the response of θ_{FP} and θ_{CP} became

random due to the complex distribution of crop canopy and partial harvest condition.

We have introduced novel new clustering schemes, $\overline{H}_{\mathrm{FP}}/\theta_{\mathrm{FP}}$ and $\overline{H}_{\mathrm{CP}}/\theta_{\mathrm{CP}}$ in this study by utilizing θ_{FP}, θ_{CP}, and the scattering entropies, H_{FP} and H_{CP}. The clustering plane is split into 12 zones, where each zone represents a distinct dominant scattering mechanism. In this regard, the $\overline{H}_{\mathrm{FP}}/\theta_{\mathrm{FP}}$ and $\overline{H}_{\mathrm{CP}}/\theta_{\mathrm{CP}}$ clustering planes provide necessary information about targets without any *apriori* knowledge of the scene.

In this context, these clustering planes was utilized to characterize phenological stages of rice. During the initial period of the growing season, a dominant odd-bounce scattering with high entropy is evident from the clusters formed in $\overline{H}_{\mathrm{FP}}/\theta_{\mathrm{FP}}$ and $\overline{H}_{\mathrm{CP}}/\theta_{\mathrm{CP}}$ plots due to the exposed soil layer for those fields. With the completion of the tillering phase, the dominant cluster density moved from the high-entropy odd-bounce scattering zone to the medium and multiple-even bounce high entropy scattering zones. This transition among the zones could be due to the stem water interaction with the incident EM wave and complex morphological characteristics of the crop canopy. At the end of the crop cycle, the entropy started to increase due to the complex canopy geometry. In contrast, the density of the clusters started shifting from even-bounce to odd-bounce zones due to partial harvest of the fields.

This study presents a meticulous analysis of θ_{FP} and θ_{CP} individually along with $\overline{H}_{\mathrm{FP}}/\theta_{\mathrm{FP}}$ and $\overline{H}_{\mathrm{CP}}/\theta_{\mathrm{CP}}$ clustering planes for rice phenology analysis. Hence, these parameters are quite useful to monitor the development of rice at each phenological stage. Besides, they also provide information

about changes in the scattering mechanism at different crop phenological stage. These parameters could be beneficial in providing essential information about crop conditions for engaging different cultivation measures. Therefore, further investigation to track and map crop growth stages could be conducted for different crop-types around the globe. The sensitivity of these parameters for different crop geometry could be examined for different incident angles using both FP and CP SAR data. We could adequately utilize these parameters for the newly launched RADARSAT Constellation Mission (RCM) and several upcoming missions.

Acknowledgements

The authors would like to thank the Canadian Space Agency and MAXAR Technologies Ltd. (formerly MDA) for providing RADARSAT-2 images through the Joint Experiment for Crop Assessment and Monitoring (JECAM) Network. The authors are also thankful to Andhra Pradesh Space Application Centre (APSAC), ITE & C Department, Government of Andhra Pradesh for their support during field campaigns. This work was supported in part by the Spanish Ministry of Science, Innovation and Universities, the State Agency of Research (AEI), and the European Funds for Regional Development (EFRD) under Project TEC 2017-85244-C 2-1-P.

References

Ainsworth, T., Kelly, J., Lee, J.-S., 2009. Classification comparisons between dual-pol, compact polarimetric and quad-pol SAR imagery. ISPRS Journal of Photogrammetry and Remote Sensing 64 (5), 464–471.

Antropov, O., Rauste, Y., Hame, T., 2011. Volume scattering modeling in PolSAR decompositions: Study of ALOS PALSAR data over boreal forest. IEEE Transactions on Geoscience and Remote Sensing 49 (10), 3838–3848.

Ballester-Berman, J. D., Lopez-Sanchez, J. M., 2011. Time series of hybrid-polarity parameters over agricultural crops. IEEE Geoscience and Remote Sensing Letters 9 (1), 139–143.

Barakat, R., 1977. Degree of polarization and the principal idempotents of the coherency matrix. Optics Communications 23 (2), 147–150.

Barakat, R., 1983. n-fold polarization measures and associated thermodynamic entropy of N partially coherent pencils of radiation. Optica Acta: International Journal of Optics 30 (8), 1171–1182.

Bouvet, A., Le Toan, T., Lam-Dao, N., 2009. Monitoring of the rice cropping system in the mekong delta using ENVISAT/ASAR dual polarization data. IEEE Transactions on Geoscience and Remote Sensing 47 (2), 517–526.

Brisco, B., Li, K., Tedford, B., Charbonneau, F., Yun, S., Murnaghan, K., 2013. Compact polarimetry assessment for rice and wetland mapping. International journal of remote sensing 34 (6), 1949–1964.

Canisius, F., Shang, J., Liu, J., Huang, X., Ma, B., Jiao, X., Geng, X., Kovacs, J. M., Walters, D., 2018. Tracking crop phenological development using multi-temporal polarimetric Radarsat-2 data. Remote Sensing of Environment 210, 508–518.

Charbonneau, F., Brisco, B., Raney, R., McNairn, H., Liu, C., Vachon, P.,

Shang, J., DeAbreu, R., Champagne, C., Merzouki, A., et al., 2010. Compact polarimetry overview and applications assessment. Canadian Journal of Remote Sensing 36 (sup2), S298–S315.

Cloude, S. R., Goodenough, D. G., Chen, H., 2011. Compact decomposition theory. IEEE Geoscience and Remote Sensing Letters 9 (1), 28–32.

Cloude, S. R., Pottier, E., 1997. An entropy based classification scheme for land applications of polarimetric SAR. IEEE transactions on geoscience and remote sensing 35 (1), 68–78.

Davidson, M. W., Le Toan, T., Mattia, F., Satalino, G., Manninen, T., Borgeaud, M., 2000. On the characterization of agricultural soil roughness for radar remote sensing studies. IEEE Transactions on Geoscience and Remote Sensing 38 (2), 630–640.

De Bernardis, C. G., Vicente-Guijalba, F., Martinez-Marin, T., Lopez-Sanchez, J. M., 2015. Estimation of key dates and stages in rice crops using dual-polarization SAR time series and a particle filtering approach. IEEE Journal of Selected Topics in Applied Earth Observations and Remote Sensing 8 (3), 1008–1018.

Dey, S., Bhattacharya, A., Ratha, D., Mandal, D., Frery, A. C., 2020. Target characterization and scattering power decomposition for full and compact polarimetric SAR data. IEEE Transactions on Geoscience and Remote Sensing.

Guo, X., Li, K., Shao, Y., Wang, Z., Li, H., Yang, Z., Liu, L., Wang, S.,

2018. Inversion of rice biophysical parameters using simulated compact polarimetric SAR C-band data. Sensors 18 (7), 2271.

He, Z., Li, S., Wang, Y., Dai, L., Lin, S., 2018. Monitoring rice phenology based on backscattering characteristics of multi-temporal RADARSAT-2 datasets. Remote Sensing 10 (2), 340.

Ji, K., Wu, Y., 2015. Scattering mechanism extraction by a modified cloude-pottier decomposition for dual polarization SAR. Remote Sensing 7 (6), 7447–7470.

Koay, J.-Y., Tan, C.-P., Lim, K.-S., bin Abu Bakar, S. B., Ewe, H.-T., Chuah, H.-T., Kong, J.-A., 2007. Paddy fields as electrically dense media: Theoretical modeling and measurement comparisons. IEEE Transactions on Geoscience and Remote Sensing 45 (9), 2837–2849.

Kumar, V., Mandal, D., Bhattacharya, A., Rao, Y., 2020. Crop characterization using an improved scattering power decomposition technique for compact polarimetric SAR data. International Journal of Applied Earth Observation and Geoinformation 88, 102052.
URL http://www.sciencedirect.com/science/article/pii/S0303243419306609

Kurosu, T., Fujita, M., Chiba, K., 1995. Monitoring of rice crop growth from space using the ERS-1 C-band SAR. IEEE Transactions on Geoscience and Remote Sensing 33 (4), 1092–1096.

Le Toan, T., Laur, H., Mougin, E., Lopes, A., 1989. Multitemporal and dual-polarization observations of agricultural vegetation covers by x-band

SAR images. IEEE transactions on geoscience and remote sensing 27 (6), 709–718.

Le Toan, T., Ribbes, F., Wang, L.-F., Floury, N., Ding, K.-H., Kong, J. A., Fujita, M., Kurosu, T., 1997. Rice crop mapping and monitoring using ERS-1 data based on experiment and modeling results. IEEE Transactions on Geoscience and Remote Sensing 35 (1), 41–56.

Lee, J.-S., Pottier, E., 2009. Polarimetric radar imaging: from basics to applications. CRC press.

Lopez-Sanchez, J. M., Ballester-Berman, J. D., Hajnsek, I., 2011. First results of rice monitoring practices in spain by means of time series of TerraSAR-X dual-pol images. IEEE Journal of selected topics in applied earth observations and remote sensing 4 (2), 412–422.

Lopez-Sanchez, J. M., Cloude, S. R., Ballester-Berman, J. D., 2012. Rice phenology monitoring by means of SAR polarimetry at X-band. IEEE Transactions on Geoscience and Remote Sensing 50 (7), 2695–2709.

Lopez-Sanchez, J. M., Vicente-Guijalba, F., Ballester-Berman, J. D., Cloude, S. R., 2014. Polarimetric response of rice fields at C-band: Analysis and phenology retrieval. IEEE Transactions on Geoscience and Remote Sensing 52 (5), 2977–2993.

Mandal, D., Kumar, V., Rao, Y., Bhattacharya, A., Ramana, K., 2019. Experimental field campaigns at Vijayawada test site. Tech. Rep. MRS2019TR02, Microwave Remote Sensing Lab, India.
URL http://doi.org/10.17605/OSF.IO/DN3E8

McNairn, H., Jiao, X., Pacheco, A., Sinha, A., Tan, W., Li, Y., 2018. Estimating canola phenology using synthetic aperture radar. Remote sensing of environment 219, 196–205.

McNairn, H., Shang, J., 2016. A review of multitemporal synthetic aperture radar (SAR) for crop monitoring. In: Multitemporal Remote Sensing. Springer, pp. 317–340.

Paloscia, S., 2002. A summary of experimental results to assess the contribution of SAR for mapping vegetation biomass and soil moisture. Canadian Journal of Remote Sensing 28 (2), 246–261.

Praks, J., Koeniguer, E. C., Hallikainen, M. T., 2009. Alternatives to target entropy and alpha angle in SAR polarimetry. IEEE Transactions on Geoscience and Remote Sensing 47 (7), 2262–2274.

Raney, R. K., 2007. Hybrid-polarity SAR architecture. IEEE Transactions on Geoscience and Remote Sensing 45 (11), 3397–3404.

Raney, R. K., Cahill, J. T., Patterson, G. W., Bussey, D. B. J., 2012. The m-chi decomposition of hybrid dual-polarimetric radar data with application to lunar craters. Journal of Geophysical Research: Planets 117 (E12).

Ratha, D., Pottier, E., Bhattacharya, A., Frery, A. C., 2019. A PolSAR scattering power factorization framework and novel roll-invariant parameter-based unsupervised classification scheme using a geodesic distance. IEEE Transactions on Geoscience and Remote Sensing, 1–17.

Sabry, R., Vachon, P. W., 2013. A unified framework for general compact and

quad polarimetric SAR data and imagery analysis. IEEE Transactions on Geoscience and Remote Sensing 52 (1), 582–602.

Torbick, N., Chowdhury, D., Salas, W., Qi, J., 2017. Monitoring rice agriculture across Myanmar using time series Sentinel-1 assisted by Landsat-8 and PALSAR-2. Remote Sensing 9 (2), 119.

Touzi, R., Hurley, J., Vachon, P. W., 2015. Optimization of the degree of polarization for enhanced ship detection using polarimetric RADARSAT-2. IEEE Transactions on Geoscience and Remote Sensing 53 (10), 5403–5424.

Touzi, R., Omari, K., Sleep, B., Jiao, X., 2018. Scattered and received wave polarization optimization for enhanced peatland classification and fire damage assessment using polarimetric PALSAR. IEEE Journal of Selected Topics in Applied Earth Observations and Remote Sensing 11 (11), 4452–4477.

Uppala, D., Kothapalli, R. V., Poloju, S., Mullapudi, S. S. V. R., Dadhwal, V. K., 2015. Rice crop discrimination using single date RISAT1 hybrid (RH, RV) polarimetric data. Photogrammetric Engineering & Remote Sensing 81 (7), 557–563.

Wiseman, G., McNairn, H., Homayouni, S., Shang, J., 2014. RADARSAT-2 polarimetric SAR response to crop biomass for agricultural production monitoring. IEEE Journal of Selected Topics in Applied Earth Observations and Remote Sensing 7 (11), 4461–4471.

Xie, L., Zhang, H., Wu, F., Wang, C., Zhang, B., 2015. Capability of rice mapping using hybrid polarimetric SAR data. IEEE Journal of Selected

769 Topics in Applied Earth Observations and Remote Sensing 8 (8), 3812–
770 3822.

771 Yang, Z., Li, K., Liu, L., Shao, Y., Brisco, B., Li, W., 2014. Rice growth mon-
772 itoring using simulated compact polarimetric C band SAR. Radio Science
773 49 (12), 1300–1315.

774 Yin, J., Moon, W. M., Yang, J., 2015. Novel model-based method for identi-
775 fication of scattering mechanisms in polarimetric SAR data. IEEE Trans-
776 actions on Geoscience and Remote Sensing 54 (1), 520–532.

777 Yin, J., Papathanassiou, K. P., Yang, J., 2019. Formalism of compact po-
778 larimetric descriptors and extension of the $\triangle\alpha B/\alpha B$ method for general
779 compact-pol SAR. IEEE Transactions on Geoscience and Remote Sensing,
780 1–14.

781 Yonezawa, C., Negishi, M., Azuma, K., Watanabe, M., Ishitsuka, N., Ogawa,
782 S., Saito, G., 2012. Growth monitoring and classification of rice fields using
783 multitemporal RADARSAT-2 full-polarimetric data. International journal
784 of remote sensing 33 (18), 5696–5711.

785 Yuzugullu, O., Erten, E., Hajnsek, I., 2015. Rice growth monitoring by means
786 of X-band co-polar SAR: Feature clustering and bbch scale. IEEE Geo-
787 science and Remote Sensing Letters 12 (6), 1218–1222.